Available online at www.sciencedirect.com
ScienceDirect
Journal of Computational Physics 218 (2006) 816–835
JOURNAL OF COMPUTATIONAL PHYSICS
www.elsevier.com/locate/jcp

High-order accurate modeling of electromagnetic wave propagation across media – Grid conforming bodies

Eugene Kashdan [1], Eli Turkel *

School of Mathematical Sciences, Department of Mathematics, Tel Aviv University, Ramat Aviv, Tel Aviv 69978, Israel

Received 11 December 2005; received in revised form 9 March 2006; accepted 9 March 2006
Available online 2 May 2006

Abstract

The Maxwell equations contain a dielectric permittivity ε that describes the particular media. For homogeneous materials at low temperatures this coefficient is constant within a material. However, it jumps at the interface between different media. This discontinuity can significantly reduce the order of accuracy of the numerical scheme. We solve the Maxwell equations, with an interface between two media, using a fourth-order accurate algorithm. We regularize the discontinuous dielectric permittivity by a continuous function either locally, near the interface, or globally, in the entire domain. We study the effect of this regularization on the order of accuracy for a one-dimensional time-dependent problem. We then implement this for the three-dimensional Maxwell equations in spherical coordinates with appropriate physical and artificial absorbing boundary conditions. We use Fourier filtering of the high frequency modes near the poles to increase the time-step.

Keywords: CEM; FDTD; Discontinuous coefficients; High-order methods; Time-dependent Maxwell equations; High-order accuracy; Discontinuities

1. Introduction

Electromagnetic waves propagate in both free space and in bodies, which may be inhomogeneous media. For instance, a cellular phone sends signals from a building to the closest antenna to register its location. Another example is a sensor that emits electromagnetic pulses into the ground to check for land mines. These can be simulated by the solution of Maxwell's equations with discontinuous coefficients. A discontinuity in coefficients occurs at an interface between media with different dielectric and magnetic properties.

* Corresponding author.
E-mail addresses: ekashdan@dam.brown.edu (E. Kashdan), turkel@post.tau.ac.il, turkel@math.tau.ac.il (E. Turkel).
[1] Presently at Brown University.

0021-9991/$ - see front matter © 2006 Elsevier Inc. All rights reserved.
doi:10.1016/j.jcp.2006.03.009

The Maxwell equations for $\vec{E}$, $\vec{D}$, $\vec{H}$ and $\vec{B}$ are:

$$\begin{aligned} &\frac{\partial \vec{B}}{\partial t} + \nabla \times \vec{E} = 0 \quad \text{(Faraday's Law)},\\ &\frac{\partial \vec{D}}{\partial t} - \nabla \times \vec{H} = -\vec{J} \quad \text{(Ampere's law)} \end{aligned} \tag{1}$$

coupled with Gauss' law

$$\nabla \cdot \vec{B} = 0, \quad \nabla \cdot \vec{D} = \rho,$$

where $\vec{J}$ is the electric current density vector and ρ is the electric charge density.

For linear materials we relate the magnetic flux density vector $\vec{B}$ to the magnetic field vector $\vec{H}$ and the electric flux density vector $\vec{D}$ to the electric field vector $\vec{E}$ using

$$\vec{B} = \mu \vec{H}, \quad \vec{D} = \varepsilon \vec{E}.$$

We assume the dielectric permittivity ε and the magnetic permeability μ are given scalar functions of space only. Both parameters are positive and describe the dielectric and magnetic characteristics of the material. We set $\varepsilon = \varepsilon_0 \cdot \varepsilon_r$ and $\mu = \mu_0 \cdot \mu_r$ where $\mu_0 = 4\pi \cdot 10^{-7} \frac{H}{m}$ and $\varepsilon_0 = \frac{1}{c^2 \mu_0} \frac{F}{m}$ are the free space permeability and permittivity, respectively ($c \approx 3.0 \times 10^8$ m/s is the speed of light). Different materials have different dielectric characteristics. For very high frequencies (more than 10 GHz) these characteristics become frequency dependent. However, for lower frequencies, at room temperature, many materials have a constant relative dielectric permittivity $\varepsilon_r \geqslant 1$ and relative permeability $\mu_r = 1$ (if they are non-metallic). In Table 1 we display ε_r for several materials.

As functions of space ε and μ may be discontinuous across the interface between different materials. This discontinuity may reduce the accuracy of a numerical scheme and may also make it unstable. The present "state-of the-art" in the numerical solution of the Maxwell equations with discontinuous coefficients by finite difference methods does not go beyond second order of accuracy confirmed for simple cases (see, for instance [1,3,7] and review in [12]). High-order accurate modelling of general dielectric bodies with meshes that are not aligned with the body remains an open challenge to be addressed in future work. Hence, in this study we shall only consider bodies aligned with the mesh.

The paper is organized as follows: We first discuss the general properties of the fourth-order accurate finite difference scheme for the solution of the time-dependent Maxwell equations and compare it to the widely used second-order accurate Yee algorithm. Afterwards, we consider the one-dimensional time-dependent Maxwell equations with piecewise continuous coefficients and describe various methods for their regularization. We compare these methods numerically and discuss the influence of the regularization on the accuracy of the finite difference scheme. Finally, we show an application of the previously discussed regularization algorithms, together with other special techniques, for the numerical solution of the three-dimensional Maxwell equations in spherical coordinates with a dielectric interface in the radial direction, i.e., the body is still aligned with the mesh.

2. Fourth-order accurate scheme

The classical finite difference time domain (FDTD) method was introduced by Yee [28] in 1966. It uses a second-order central difference scheme for integration in space and the second-order leapfrog scheme for

Table 1
Relative permittivities for different materials

Material/medium	ε_r
Air	1.0
Ice (at 0 °C)	3.2
Distilled water	80.0
Silica glass	2.25
Teflon	2.1
Rubber	2.3–4

integration in time. This is a staggered non-dissipative scheme in both space and time. This method is implemented in most of the commercial and open source solvers of the time-dependent Maxwell equations. However, because of the second-order accuracy, it requires a dense grid to model various scales. This dense mesh reduces the allowable time-step since stability requirements demand that the time-step be proportional to the spatial mesh size. Hence, a fine mesh requires both a lot of computer storage and also a long computer running time. If we define N as the maximal number of grid points in one direction, then for the three-dimensional problem the storage will grow with $O(N^3)$ and the computational cost with $O(N^4)$.

Instead, we implement a fourth-order accurate FDTD scheme for the solution of the Maxwell equations suggested by Yefet and Turkel [30]. This scheme has a number of advantages over the second-order scheme (see, for instance, [12,25]). The high order method only needs a coarse grid. This is especially important for three-dimensional numerical simulations and for long time integrations. A comparison of different fourth-order schemes can be found in [18,25].

There are several ways to treat a discontinuity for high-order accurate schemes. The important question is how to preserve the global order of accuracy. One of the approaches to the solution of Maxwell equations is based on one-sided finite difference formulae, approximating the differential equation from both sides of the interface (see, for example, [7]). However, for multi-dimensional problems it is difficult to achieve higher-order accuracy for an interface not aligned with the grid. Another drawback of this approach is the violation of Gauss' law at the interface that can lead to the spurious solutions (see, for example, [16]).

2.1. Spatial discretization

The scheme we use to approximate the spatial derivatives is a compact implicit scheme with the same staggering as the Yee scheme. Gottlieb and Yang [11] and Turkel [25] have shown that a staggered scheme is more accurate than a co-located scheme for the same order of accuracy (it has smaller constant in the error term). Staggering also simplifies the construction of the boundary conditions when fewer components are located on boundaries. The compact implicit scheme is a good compromise between an unconditionally stable implicit scheme that requires the inversion of large dense matrices and an explicit scheme that has a stability condition imposed on the time-step. The scheme in one dimension is derived using a Taylor expansion (see also [26]):

$$\frac{u_{i+1/2}-u_{i-1/2}}{h}=u_i'+\frac{h^2}{24}D_{hh}(u_i')+O(h^4),$$

where $D_{hh}=\frac{(*)_{i+1}-2(*)_i+(*)_{i-1}}{h^2}$ is a second-order accurate finite difference operator for approximation of second derivative. A fourth-order compact implicit scheme for the approximation of the spatial derivatives is then derived [26] as in Fig. 1:

$$\frac{(Du)_{i+1}+(Du)_{i-1}}{24}+\frac{11}{12}(Du)_i=\frac{u_{i+\frac{1}{2}}-u_{i-\frac{1}{2}}}{\Delta x}. \tag{2}$$

At the first and last nodes and half-nodes we use fourth-order accurate one-sided approximations based on the operators:

$$D_{hh}^1=\frac{2(*)_1-5(*)_2+4(*)_3-(*)_4}{h^2},\quad D_{hh}^p=\frac{2(*)_p-5(*)_{p-1}+4(*)_{p-2}-(*)_{p-3}}{h^2}.$$

The total spatial portion of the scheme, in matrix form, is given in Fig. 1.

$$\frac{1}{24}\begin{bmatrix}26&-5&4&-1&.&.&0\\1&22&1&0&.&.&0\\0&1&22&1&0&.&0\\.&.&.&.&.&.&.\\0&.&.&0&1&22&1\\0&.&.&-1&4&-5&26\end{bmatrix}\frac{\partial}{\partial *}\begin{bmatrix}U_1\\U_2\\.\\.\\U_{p-2}\\U_{p-1}\end{bmatrix}=\frac{1}{\Delta *}\begin{pmatrix}U_{3/2}-U_{1/2}\\U_{5/2}-U_{3/2}\\.\\.\\U_{p-5/2}-U_{p-3/2}\\U_{p-3/2}-U_{p-1/2}\end{pmatrix}\qquad \frac{1}{24}\begin{bmatrix}26&-5&4&-1&.&.&0\\1&22&1&0&.&.&0\\0&1&22&1&0&.&0\\.&.&.&.&.&.&.\\0&.&.&0&1&22&1\\0&.&.&-1&4&-5&26\end{bmatrix}\frac{\partial}{\partial *}\begin{bmatrix}U_{1/2}\\U_{3/2}\\.\\.\\U_{p-3/2}\\U_{p-1/2}\end{bmatrix}=\frac{1}{\Delta *}\begin{pmatrix}U_1-U_0\\U_2-U_1\\.\\.\\U_{p-1}-U_{p-2}\\U_p-U_{p-1}\end{pmatrix}$$

Fig. 1. Approximation of the spatial derivatives at the nodes/half-nodes.

Here "$*$" denotes the direction of differentiation, p is the number of grid points in one direction and U is a differentiated component of the Maxwell equations. Carpenter et al. [5,6] have shown in a similar case that the scheme is stable in spite of the one-sided stencil near the boundary. This scheme uses the same 3-point stencil as Yee scheme. The almost tridiagonal system is solved using an LU decomposition (Thomas' algorithm) with O(N) operations.

Yefet [29] gives a comparative analysis of the fourth-order compact implicit scheme and the second-order central difference scheme used in the Yee algorithm. He found that the compact implicit scheme as well as the Yee scheme (see also [22]) have pure imaginary eigenvalues so both schemes are non-dissipative but dispersive. Kashdan and Galanti [19] discuss an effective parallelization strategy for the compact implicit scheme applied to the spatial discretization of the three-dimensional time-dependent Maxwell equations based on an alternating domain decomposition.

2.2. Fourth-order approximation of the temporal derivative

For integration in time we replace the second-order leapfrog scheme by a fourth-order accurate Runge–Kutta scheme (f is a spatial finite difference operator):

$$\begin{aligned} U^{(1)} &= U^n + \frac{\Delta t}{4} f[U^{(n)}], \\ U^{(2)} &= U^n + \frac{\Delta t}{3} f[U^{(1)}], \\ U^{(3)} &= U^n + \frac{\Delta t}{2} f[U^{(2)}], \\ U^{(n+1)} &= U^n + \Delta t f[U^{(3)}]. \end{aligned} \tag{3}$$

This is a co-located, in time, second-order accurate scheme for general ODEs, but preserves fourth-order accuracy for linear equations [31].

We have the following comparison of the four-stage Runge–Kutta method (3) versus the leapfrog scheme [25]:

(1) *Time-step*. Without staggering in time, (3) has a time-step (CFL condition) that is potentially 2.8 times larger than leapfrog. Since the Yee algorithm is staggered in time, the Runge–Kutta scheme loses a factor of two, but still has a time-step 1.4 larger. The Runge–Kutta scheme requires four times more computations per time-step than leapfrog.
(2) *Dissipation*. The leapfrog method is not dissipative, while the four-stage Runge–Kutta scheme is dissipative. Dissipativity of the scheme causes a leak of energy from the system. However, this dissipation helps to stabilize the numerical solution in simulations of high frequency wave propagation. The Runge–Kutta scheme is in general more robust especially at discontinuities.
(3) *Numerical dispersion*. Both schemes are dispersive. The leapfrog scheme has a phase lead for time-steps within the stability limit. The Runge–Kutta scheme has either phase lag or phase lead depending on the choice of the time-step. For time-steps near the CFL limit there is a phase lag.

3. One-dimensional time-dependent problem

Our goal is to build a three-dimensional time-dependent code for simulations of electromagnetic phenomena in various media. This requires the analysis of the order of convergence, stability and robustness of the numerical scheme. This analysis is easier in one dimension though the applications are to three-dimensional time-dependent wave propagation. Hence, we consider the system of the one-dimensional Maxwell equations:

$$\varepsilon \frac{\partial E}{\partial t} = \frac{\partial H}{\partial x}, \quad \mu \frac{\partial H}{\partial t} = \frac{\partial E}{\partial x}. \tag{4}$$

As the material interface model we consider a dielectric body (ε_2) surrounded by free space ($\varepsilon_1 = \mu_1 = 1$) as shown in Fig. 2.

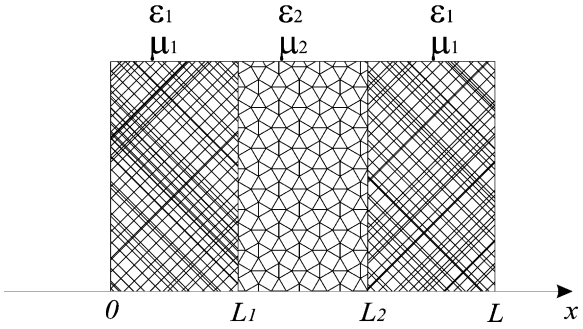

Fig. 2. Two interface model.

At each interface L_1 and L_2 we supplement (4) by the jump conditions:

$$\begin{aligned} &E^+ = E^-, && H^+ = H^-, \\ &\left(\tfrac{1}{\mu}\tfrac{\partial E}{\partial x}\right)^+ = \left(\tfrac{1}{\mu}\tfrac{\partial E}{\partial x}\right)^-, && \left(\tfrac{1}{\varepsilon}\tfrac{\partial H}{\partial x}\right)^+ = \left(\tfrac{1}{\varepsilon}\tfrac{\partial H}{\partial x}\right)^-. \end{aligned} \tag{5}$$

The one-dimensional model shown in Fig. 2 can be considered as a part of the periodically structured dielectric media. An example of such media is photonic crystals (see, for example, [17]). These artificial materials are used in devices ranging from dielectric mirrors and reflective coatings to DFB lasers.

4. Regularization of discontinuous functions

The idea of regularization is the replacement of the discontinuous function by a continuous approximation. We develop our algorithm based on this approach. A straightforward calculation shows that a central difference scheme preserves a zero divergence of $\vec{E}$ or $\vec{B}$ Gauss' Law even when the coefficients vary spatially. An important question is what function to regularize: ε or $\frac{1}{\varepsilon}$, μ or $\frac{1}{\mu}$. Regularization is based on averaging of the piecewise-continuous function at the discontinuity. However, algebraic, geometric and harmonic averages yield different values which affect the accuracy of the numerical solution. Another aspect of the regularization is connected to the angle of incidence of the electromagnetic wave to the interface. Andersson [1] shows, using the integral formulation of Ampere's Law, that in order to preserve the second-order accuracy of the Yee scheme the tangential, to the interface, components should be approximated using arithmetic averaging. On the other hand, for the normal components the harmonic averaging should be used.

The electric and magnetic field vectors are mutually perpendicular. So one should use different types of averaging when both ε and μ are discontinuous at the interface. We divide regularization techniques into local and global methods. We also pay attention as to whether the regularization should be monotonic.

We denote the errors by Q since E represents the electric field. The numerical implementation of regularization introduces two types of errors: Q_1 is the error caused by replacement of the discontinuous problem by the regularized problem (''regularization error'') and Q_2 the error from the numerical discretization of the regularized problem (''numerical error''). The total error is $Q_1 + Q_2$. Clearly, Q_1 becomes smaller when the length of the regularization region decreases ($\delta \to 0$). However, $\delta \to 0$ increases the error Q_2. The behavior of both regularization and numerical errors as a function of the grid resolution was studied by Kashdan in [18]. A numerical and asymptotic study of high-order accurate methods for the solution of the frequency space Maxwell equations and Helmholtz equation with discontinuous coefficients is given by Kashdan in [18] and Kashdan and Turkel in [20].

4.1. Local regularization

4.1.1. Simple averaging

Consider simple averaging of the dielectric permittivity ε at the discontinuity as a particular case of local regularization. We choose several types of averaging:

- arithmetic averaging: $\varepsilon(L_1) = \varepsilon(L_2) = 0.5(\varepsilon_1 + \varepsilon_2)$;
- harmonic averaging: $\varepsilon(L_1) = \varepsilon(L_2) = \frac{2\varepsilon_1\varepsilon_2}{(\varepsilon_1+\varepsilon_2)}$.

4.1.2. Hermite cubic spline

We choose ε as either ε_1 or ε_2 far away from the discontinuities (see Fig. 2). We choose $\delta > 0$ and connect ε_1 and ε_2 with a smooth function for $|x - x_0| < \delta$. We also connect ε smoothly to the constant states at $x - x_0 = \pm\delta$. As an example of a connecting function we construct the Hermite cubic spline. Any cubic spline can be written as

$$\varepsilon(x) = c_1 + c_2(x - x_k) + c_3(x - x_k)^2 + c_4(x - x_k)^3. \tag{6}$$

We then define in the interval $x_{k-1/2} \leqslant x \leqslant x_{k+1/2}$ the following parameters:

$$\begin{aligned} c_1 &= f_{k+1/2}, \\ c_2 &= f'_{k+1/2}, \\ c_3 &= \frac{3S_k - f'_{k+1/2} - 2f'_{k-1/2}}{\Delta x}, \\ c_4 &= -\frac{2S_k - f'_{k+1/2} - f'_{k-1/2}}{(\Delta x)^2} \end{aligned}$$

and

$$S_k = \frac{f_{k+1/2} - f_{k-1/2}}{\Delta x},$$

where f is equal to ε at the half-nodes. These conditions are derived in [15], where it is shown that the most accurate approximation can be achieved if the derivative f' is approximated using a high-order accurate implicit finite difference scheme.

We try improving the quality and accuracy of the approximation by enforcing monotonicity to remove non-physical oscillations. The following criteria, [15], allows the addition of a monotonicity restraint to the approximation

$$f'_k = \begin{cases} \min[\max(0, f'_k), 3\min(S_{k-1}, S_k)], & \min(S_{k-1}, S_k) > 0, \\ \max[\min(0, f'_k), 3\max(S_{k-1}, S_k)], & \max(S_{k-1}, S_k) < 0, \\ 0, & S_{k-1} \cdot S_k \leqslant 0. \end{cases} \tag{7}$$

4.1.3. High-order polynomial

As an alternative to a cubic spline one can consider a high-order polynomial smoothly connecting the known ε_l and ε_r at a distance δ from the interfaces. Let $z = \frac{x-x_0}{\delta}$ be the normalized distance from the interface x_0. We define the polynomial

$$\varepsilon(x) = \frac{\varepsilon_l + \varepsilon_r}{2} + \frac{\varepsilon_l - \varepsilon_r}{2}\frac{315}{128}z\left(1 - \frac{4z^2}{3} + \frac{6z^4}{5} - \frac{4z^6}{7} + \frac{z^8}{9}\right), \tag{8}$$

where $f(x)$ and its first four derivatives are continuous at $x_0 - \delta$ and $x_0 + \delta$. Moreover, this function is monotone since $f' = \frac{315}{128}(1 - z^2)^4 \geqslant 0$ for $-1 \leqslant z \leqslant 1$.

4.1.4. Vanishing of moments

Tornberg and Engquist [24], for the Poisson equation, and Andersson and Engquist [2], for the Maxwell equations, have presented a local regularization technique based on polynomial connecting functions that satisfy one or more vanishing moment conditions:

$$M_n = \int_{-\delta}^{\delta} [\varepsilon - \varepsilon(x)]x^n \, dx = 0, \quad n \geqslant 0. \tag{9}$$

In the numerical experiments in [2] the authors used linear, third-order and fifth-order polynomials satisfying the vanishing of up to four moments (9).

4.2. Global regularization

For global regularization (ε approximated throughout the physical domain) by an implicit fourth-order accurate (Padé) interpolation. Based on a Taylor expansion we have:

$$\frac{f_{i+1/2}+f_{i-1/2}}{2} = f_i + \frac{h^2}{8} f_i'' + \mathrm{O}(h^4),$$
$$\frac{f_{i+1}+f_{i-1}}{2} = f_i + \frac{h^2}{2} f_i'' + \mathrm{O}(h^4).$$

Eliminating the error term we obtain

$$\frac{f_{i+1}+f_{i-1}}{8} + \frac{3}{4} f_i = \frac{f_{i+1/2}+f_{i-1/2}}{2} + \mathrm{O}(h^4). \tag{10}$$

In the first and the last rows (away from the interface) a one-sided third-order accurate approximation is used according to:

$$\begin{aligned} \frac{-5f_2+4f_3-f_4}{8} + \frac{5}{4} f_1 &= \frac{f_{1/2}+f_{3/2}}{2}, \\ \frac{-f_{p-4}+4f_{p-3}-5f_{p-2}}{8} + \frac{5}{4} f_p &= \frac{f_{p-3/2}+f_{p-1/2}}{2}. \end{aligned} \tag{11}$$

We choose $f = \varepsilon$. The algorithm uses a tridiagonal solver to find the new values of ε. Hence, the updated ε at a single node depends on the original ε at all the grid points. This does not necessarily preserve monotonicity.

5. Experimental results

5.1. Model problem I

For most physical systems μ is fairly constant across an interface. However, for μ constant and variable ε there is, in general, no explicit solution to be used for calculating errors. Hence, for mathematical reasons, we consider the case $\mu = \varepsilon$. The explicit solution of the Maxwell system (4) is then given by:

$$\begin{aligned} E(x,t) &= A \cdot f\left(t + \int_0^x \varepsilon(s)\,\mathrm{d}s\right) + B \cdot g\left(t - \int_0^x \varepsilon(s)\,\mathrm{d}s\right), \\ H(x,t) &= A \cdot f\left(t + \int_0^x \varepsilon(s)\,\mathrm{d}s\right) - B \cdot g\left(t + \int_0^x \varepsilon(s)\,\mathrm{d}s\right), \end{aligned} \tag{12}$$

where ε can be approximated by the analytic function:

$$\varepsilon(x) \approx \varepsilon(x,\eta) = \varepsilon_1 + (\varepsilon_2 - \varepsilon_1)\frac{\tanh[\eta(x-L_1)] - \tanh[\eta(x-L_2)]}{\tanh(\eta L_1) + \tanh(\eta L_2)}, \quad -\infty < x < \infty.$$

In Fig. 3 we present ε as function of x for various η.

Numerical experiments [18] show that for $\eta \geqslant 100$ further increasing η changes the solution on the level of the machine error. In the numerical experiments we set $\eta = 200$ for calculating the exact solution. We choose $L = 4\pi$, $L_1 = 0.375L$, $L_2 = 0.625L$. We study the connection between the accuracy of the numerical scheme and the size of the jump in ε on the interface. We choose $\varepsilon_2 = 3, 7, 11$ and compare the errors in the numerical solution on grids with 129, 257 and 513 nodes. We choose the explicit solution as:

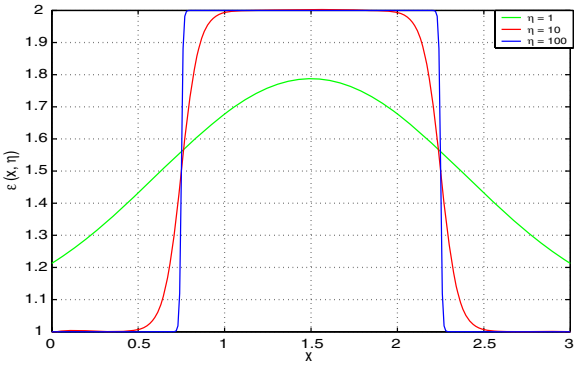

Fig. 3. Approximation of relative permittivity by continuous function for model problem.

$$E = \sin\left(t + \int_0^x \varepsilon(s)\,\mathrm{d}s\right) - \sin\left(t - \int_0^x \varepsilon(s)\,\mathrm{d}s\right) = 2\cos(t)\sin\left(\int_0^x \varepsilon(s)\,\mathrm{d}s\right),$$
$$H = \sin\left(t + \int_0^x \varepsilon(s)\,\mathrm{d}s\right) + \sin\left(t - \int_0^x \varepsilon(s)\,\mathrm{d}s\right) = 2\sin(t)\cos\left(\int_0^x \varepsilon(s)\,\mathrm{d}s\right). \tag{13}$$

The initial conditions are given by (13) with $t = 0$. This solves Maxwell's equations (4) together with the jump conditions (5). We solve numerically the dimensionless equations ($c = 1$) and E and H are normalized to have the same magnitude. In the following plots we show the L_2 error of the approximation of E as function of time. The error in H behaves similarly. We locate the interface at a node so only the electric field component is located on interface. The "regularization" error Q_1 between the continuous solution based on variable ε and piecewise continuous ε (denoted as $\varepsilon_{\lim}$) is given by

$$Q_1 = \left\| 2\cos(t)\left[\sin\left(\int_0^x \varepsilon(s)\,\mathrm{d}s\right) - \sin\left(\int_0^x \varepsilon_{\lim}(s)\,\mathrm{d}s\right)\right]\right\| \leqslant 4\left\|\sin\left[\int_0^x \frac{\varepsilon(s) - \varepsilon_{\lim}(s)}{2}\,\mathrm{d}s\right]\right\|. \tag{14}$$

We have verified that for constant ε the scheme discussed in Section 2 is fourth-order accurate. However, we expect a reduction of accuracy driven by the regularization of the piecewise continuous permittivity.

5.1.1. Averaging

We compare the arithmetic and harmonic averaging of ε on the interface for both the Yee and the fourth-order algorithm.

In all the figures in this section we display the error between the numerical solution and the solution of the original continuous problem with piecewise constant coefficients, i.e., the total error.

One observes from Figs. 4 and 5 that arithmetic averaging reduces the order of accuracy to second for fourth-order scheme and to 1.5 for Yee scheme. The harmonic averaging is only first order accurate, both independent of the size of the jump. As expected, the L_2 error of Yee scheme is larger than the error of the fourth-order scheme for the same grid resolution. Hence, even when a discontinuity occurs it is more efficient to use the fourth-order implicit scheme rather than Yee scheme.

5.1.2. Spline

A study of the local regularization in [18] shows that the physical length of the δ-interval can be chosen the same for all the grids. In all the numerical tests in this work we choose $\delta = \pi/32$. This allows the use of at least four points from the discontinuity for the spline construction. We compare the regularization with and without the monotonicity restraint on the spline as given by (7).

The plots in Fig. 6 show that local regularization with splines is second-order accurate and confirms the results from the frequency domain given in [18,20]. The monotonicity restraint does not improve the error behavior and order of accuracy.

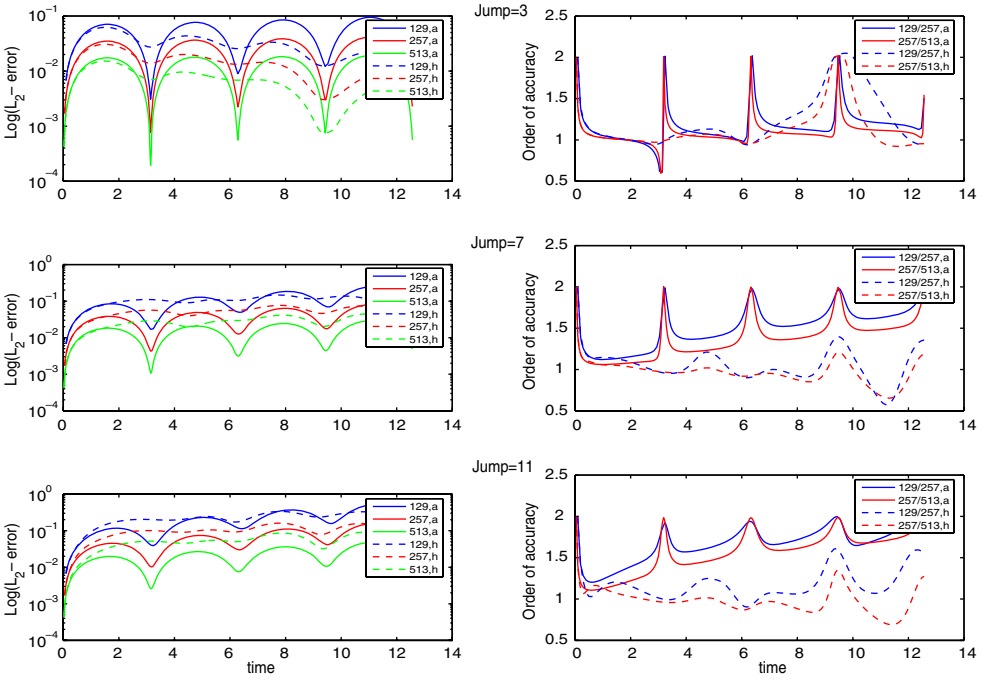

Fig. 4. Arithmetic (a) and harmonic (h) averaging of εs on interface, Yee scheme.

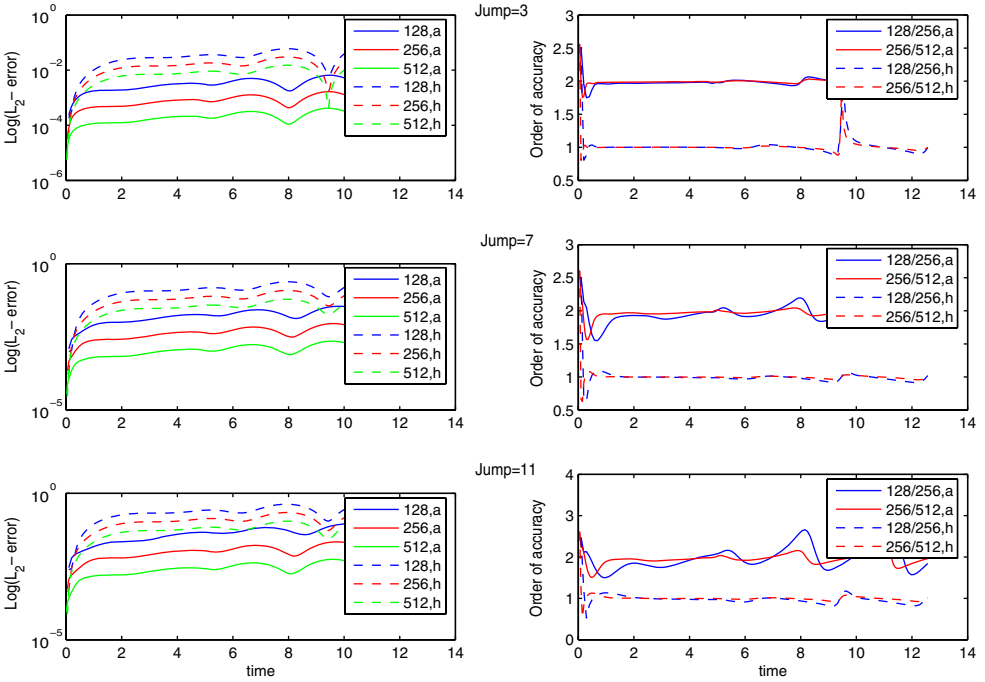

Fig. 5. Arithmetic (a) and harmonic (h) averaging of ε on interface, fourth order scheme.

5.1.3. High-order polynomial

We choose two kinds of δ-interval: fixed physical length for all grids $\delta = \pi/32$ and four mesh points but variable physical length. At the edges of the regularization region, the high-order polynomial is smoother than

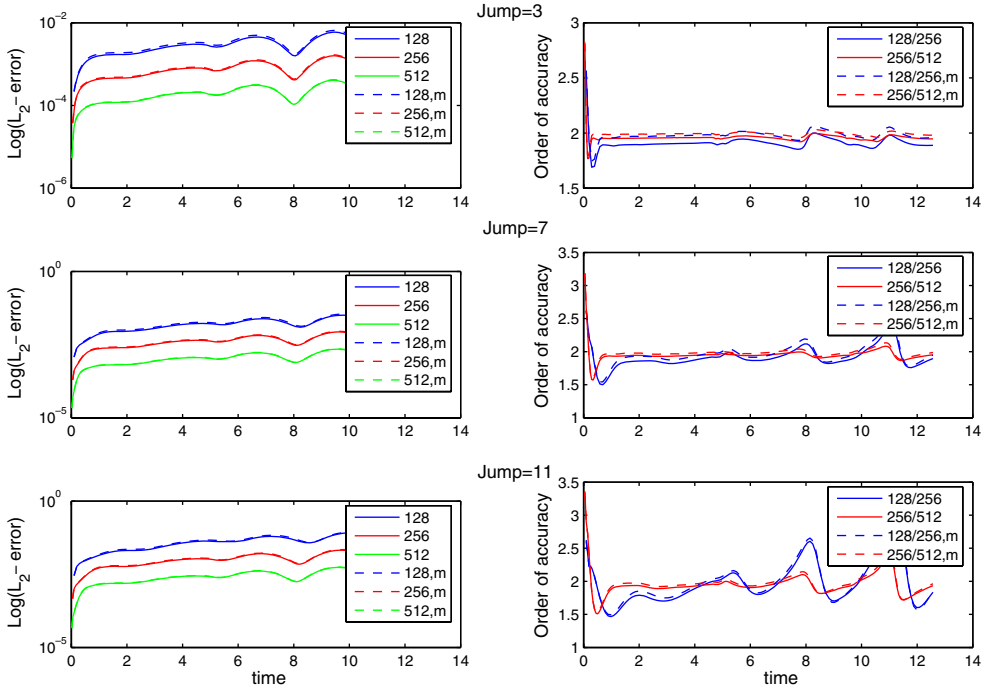

Fig. 6. Regularization of ε by Hermite cubic spline w/wo monotonicity restraint (m).

the cubic Hermitian spline. However, in the interior of the regularization region the spline is closer to the original piecewise continuous function.

One observes from Fig. 7 that the regularization of the discontinuous function with a high-order polynomial is only second-order accurate for the variable physical length of the δ-interval and the method does not converge to the analytic solution when the physical length of the δ-interval is fixed (more points are used for construction of the polynomial on grids with increasing resolution). We conclude that a high-order monotonic polynomial yields results similar to that for the cubic spline for variable physical length of δ-region. Hence, monotonicity is not important. Furthermore, the requirement of four continuous derivatives on the boundaries of the δ-interval seems to be unnecessary.

The numerical experiments in [2], using a fourth-order accurate scheme with a local regularization based on the vanishing moments condition (9), lead the authors to similar accuracy observations. The order of accuracy is reduced, with subsequent mesh refinement, to 1.5–2 even when preserving high-order moments. In [20] it is conjectured that the reason for the lower-order accuracy for very fine meshes is that the optimal regularization occurs within one mesh width and so is not represented by a standard finite difference technique.

5.1.4. Global regularization

We next apply an implicit fourth-order accurate (Padé) interpolation as given by (10) + (11) to regularize ε and $1/\varepsilon$. The CFL condition for the largest discontinuity is set equal to 0.5 because of stability considerations. The plots in Fig. 8 show that the global regularization of ε allows an average order of accuracy of 2.8, while the regularization of $1/\varepsilon$ is only second-order accurate. For the largest jumps the regularization of $1/\varepsilon$ yields an unstable solution.

Finally, we apply Padé interpolation with the second-order accurate Yee scheme. Comparing simple averaging (Fig. 4) with global regularization for Yee's scheme (Fig. 9) one observes that global regularization of ε yields an improvement in accuracy especially for large jumps. Global regularization based on $1/\varepsilon$, with the Yee scheme, does not converge to the analytic solution. Comparing Fig. 9 to Fig. 8 we see that the compact implicit scheme is always much more accurate than the Yee scheme. The oscillating behavior of the error in time for the Yee scheme (Figs. 4 and 9) is caused by numerical dispersion. On the other hand the fourth-order scheme

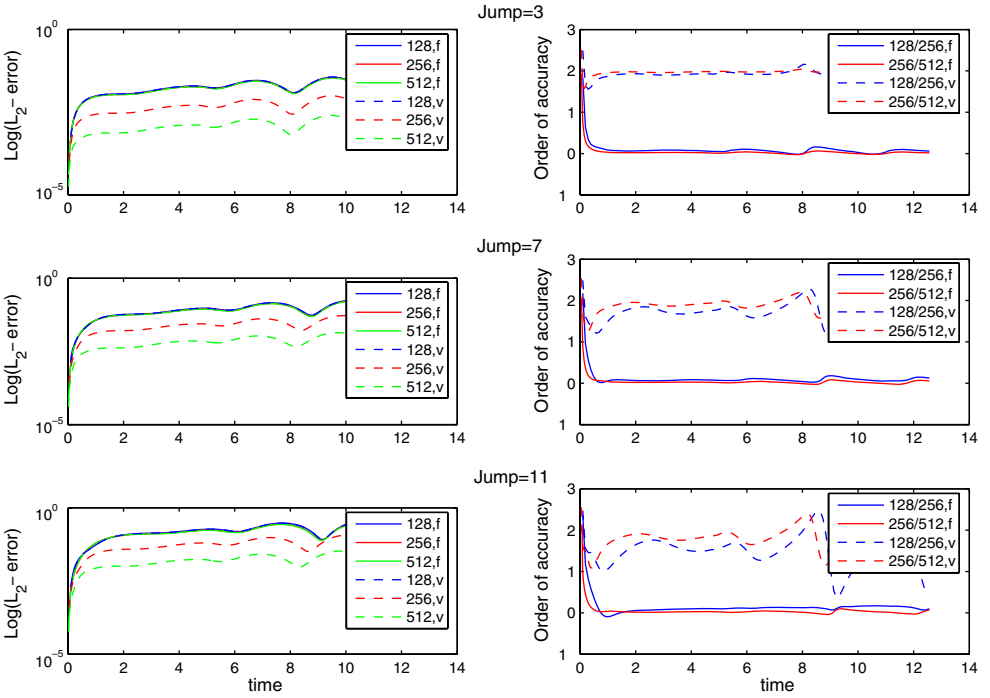

Fig. 7. Regularization of dielectric permittivity on interface by high-order polynomial with fixed (f) and variable (v) length of δ-interval.

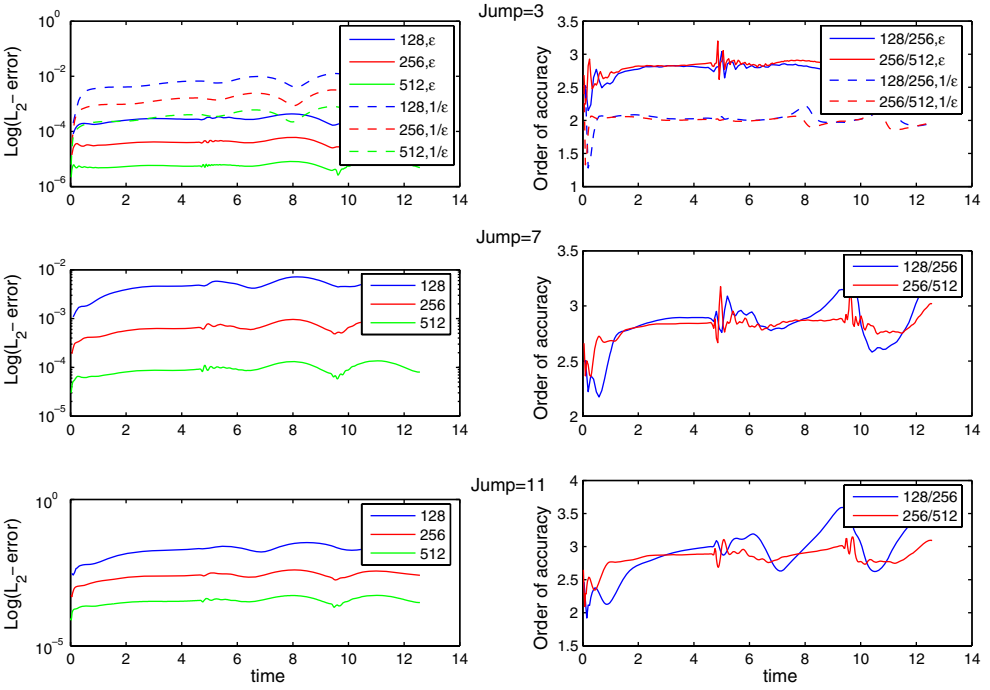

Fig. 8. Global regularization of ε and $1/\varepsilon$ using Padé interpolation.

has much better dispersive characteristics and a smaller truncation error [29]. From formula (14) we see that the regularization error is time dependent. Therefore, the balance error between the regularization error and the discretization error varies in time for a given grid.

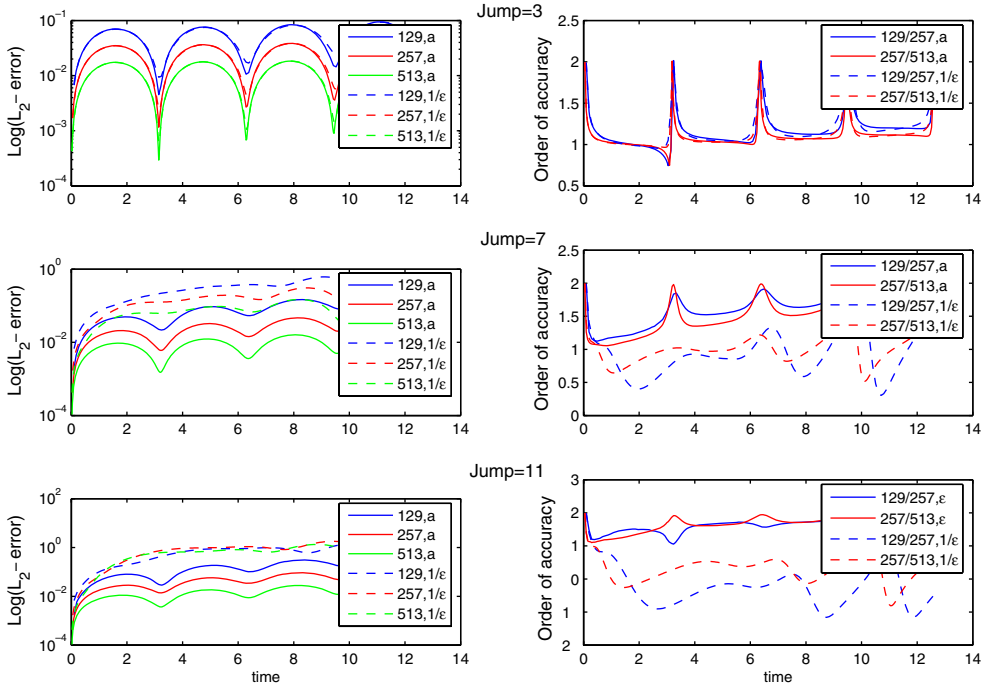

Fig. 9. Global regularization of ε and $1/\varepsilon$ using Padé interpolation for Yee scheme.

5.1.5. Estimation of the regularization error

As shown in [18,20], the regularization error Q_1 (see Section 4), caused by the replacement of the problem with a piecewise continuous coefficient by a smooth function, may reduce the order of accuracy. For fine grids the regularization error is a large percentage of the total error. In order to estimate the regularization error we substitute the regularized ε into the first of Eq. (13) and approximate the indefinite integral using a Newton–Bessel interpolation with order of accuracy $O(\Delta x^7)$, which is more than sufficient for our needs. This is then compared with the explicit solution for the piecewise continuous ε (see also (14)).

Table 2 shows the Q_1 error for global regularization of ε, i.e., the error between the analytic solution of the continuous problem with discontinuous coefficients and the analytic solution of the continuous regularized problem, see (14). We also list the order of convergence and the ratio (percent) of the regularization error to the total error. We define rate as the relation between errors on two consecutive grids and display the order of convergence as $\log_2(\text{rate})$.

Table 2 shows that the role played by the regularization error increases with the mesh refinement. For very dense grids, when the total error is dominated by the regularization error, the order of convergence of global

Table 2
Regularization (Q_1) error for various ε_2

ε_2	Number of nodes	Δx	$\|Q_1\|_{L_2}$	Rate	Order of convergence	Percent in total error
3	129	0.098	1.6094×10^{-4}			30.3
	257	0.049	2.8777×10^{-5}	5.5927	2.4835	37.4
	513	0.025	5.1017×10^{-6}	5.6406	2.4958	48.8
7	129	0.098	9.9137×10^{-4}			13.9
	257	0.049	1.8864×10^{-4}	5.2554	2.3938	19.6
	513	0.025	3.3989×10^{-5}	5.5500	2.4749	24.9
11	129	0.098	2.2362×10^{-3}			6.7
	257	0.049	4.7243×10^{-4}	4.7333	2.2428	12.1
	513	0.025	8.7584×10^{-5}	5.3941	2.4314	16.6

regularization is limited by 2.5. When the jump in ε increases at the material interface, the total error increases and the numerical error Q_2 is the main factor in the total error.

5.2. Model problem II

We consider the more realistic case, where μ is constant and only ε is discontinuous. Consider $\mu_1 = \mu_2 = 1$ and ε_2 equal to 2, 5 and 10. Choose, in Fig. 2, $L = 12$, $L_1 = 0.375L$, $L_2 = 0.625L$. We solve the one-dimensional Maxwell equations with an initial field of the form:

$$E(x,0) = \begin{cases} 0, & 0 < x < x_1, \\ f(x), & x_1 \leqslant x \leqslant x_2, \\ 0, & x > x_2, \end{cases}$$
$$H(x,0) = 0.$$

The signal is $f(x) := A \cdot [\sin(x - x_1) \cdot \sin(x - x_2)]^4$, $x_1 \leqslant x \leqslant x_2$, and zero otherwise. This is a smooth function with compact support. We no longer have an explicit solution with discontinuous ε and these initial/boundary conditions.

The physical domain $[0,L]$ is surrounded by a perfect electric conductor (PEC), $E(0) = E(L) = 0$. Since we no longer have an explicit solution we base the error on the numerical solution for a very fine grid. Based on model problem I we expect convergence and so this is reasonable. We compare the numerical solution on grids with 129, 257 and 513 nodes inside the physical domain with the "reference" solution, to the original piecewise constant coefficient problem, constructed on a very fine grid with 2049 nodes. We compare the solutions at the analytically computed time when the right moving wave reaches the end of the physical domain ($t = 9$).

For the global regularization we approximate ε using the scheme (10) + (11). The CFL condition is chosen 0.5 for largest jump in ε. For local regularization we use a Hermite cubic spline (6) as the connecting function without the monotonicity restraint (7). All regularizations are for ε and not $\frac{1}{\varepsilon}$.

Table 3
Total error using global regularization for various ε_2

ε_2	Number of nodes	Δx	$\|\text{Error}\|_{L_2}$	Rate	Order of accuracy
2	129	0.094	2.7×10^{-3}		
	257	0.047	2.4674×10^{-4}	11.0106	3.4608
	513	0.023	3.4487×10^{-5}	7.1547	2.8389
5	129	0.094	5.8×10^{-3}		
	257	0.047	6.3582×10^{-4}	9.0530	3.1784
	513	0.023	1.1239×10^{-4}	5.6574	2.5001
10	129	0.094	9.4×10^{-3}		
	257	0.047	9.0180×10^{-4}	10.3760	3.3752
	513	0.023	1.8947×10^{-4}	4.7596	2.2508

Table 4
Total error using local regularization for various ε_2

ε_2	Number of nodes	Δx	$\|\text{Error}\|_{L_2}$	Rate	Order of accuracy
2	129	0.094	3.0×10^{-3}		
	257	0.047	3.3194×10^{-4}	9.0704	3.1812
	513	0.023	6.2276×10^{-5}	5.3301	2.4142
5	129	0.094	6.8×10^{-3}		
	257	0.047	1.0×10^{-3}	6.7146	2.7473
	513	0.023	2.1249×10^{-4}	4.7563	2.2499
10	129	0.094	1.2×10^{-3}		
	257	0.047	2.0×10^{-3}	6.1268	2.6151
	513	0.023	4.0399×10^{-4}	4.8496	2.2779

From Table 3 we see that the numerical scheme has an order of accuracy higher than three for the coarse grids. However, it is reduced to second order for the finest mesh of 513 nodes. Comparing Tables 3 and 4 we observe that global regularization yields the smaller error.

6. 3D computations

6.1. Formulation of the 3D problem

Any coordinate system that is not aligned with the bodies has the disadvantage that the body cannot be represented exactly. A general body in a Cartesian coordinate system gives rise to stair-casing and its resultant errors (see, for instance, [4,14]). In this paper we only consider bodies aligned with the coordinate system and so staircasing does not occur. Consider a PEC sphere surrounded by two different homogeneous media separated with an interface in the radial direction. Each medium has its own dielectric permittivity ε (the outermost medium is free space). This problem shown in Fig. 10 has no explicit solution.

The Maxwell equations in spherical coordinates (r,θ,φ) are given by:

$$\begin{aligned}
\varepsilon\frac{\partial E_r}{\partial t} &= \frac{1}{r\sin\theta}\left[\frac{\partial}{\partial\theta}(\sin\theta H_\varphi) - \frac{\partial H_\theta}{\partial\varphi}\right],\\
\varepsilon\frac{\partial E_\theta}{\partial t} &= \frac{1}{r\sin\theta}\frac{\partial H_r}{\partial\varphi} - \frac{1}{r}\frac{\partial}{\partial r}(rH_\varphi),\\
\varepsilon\frac{\partial E_\varphi}{\partial t} &= \frac{1}{r}\left[\frac{\partial}{\partial r}(rH_\theta) - \frac{\partial H_r}{\partial\theta}\right],\\
\mu\frac{\partial H_r}{\partial t} &= -\frac{1}{r\sin\theta}\left[\frac{\partial}{\partial\theta}(\sin\theta E_\varphi) - \frac{\partial E_\theta}{\partial\varphi}\right],\\
\mu\frac{\partial H_\theta}{\partial t} &= -\frac{1}{r\sin\theta}\frac{\partial E_r}{\partial\varphi} + \frac{1}{r}\frac{\partial}{\partial r}(rE_\varphi),\\
\mu\frac{\partial H_\varphi}{\partial t} &= -\frac{1}{r}\left[\frac{\partial}{\partial r}(rE_\theta) - \frac{\partial E_r}{\partial\theta}\right].
\end{aligned} \tag{15}$$

In addition to the time dependent equations we have Gauss' law. In the absence of sources both the divergence of $\vec{E}$ and $\vec{H}$ are zero:

$$\begin{aligned}
\operatorname{div}\vec{E} &= \frac{1}{r}\frac{\partial}{\partial r}(r^2E_r) + \frac{1}{r\sin\theta}\frac{\partial}{\partial\theta}(\sin\theta E_\theta) + \frac{1}{r\sin\theta}\frac{\partial E_\varphi}{\partial\varphi} = 0,\\
\operatorname{div}\vec{H} &= \frac{1}{r}\frac{\partial}{\partial r}(r^2H_r) + \frac{1}{r\sin\theta}\frac{\partial}{\partial\theta}(\sin\theta H_\theta) + \frac{1}{r\sin\theta}\frac{\partial H_\varphi}{\partial\varphi} = 0.
\end{aligned} \tag{16}$$

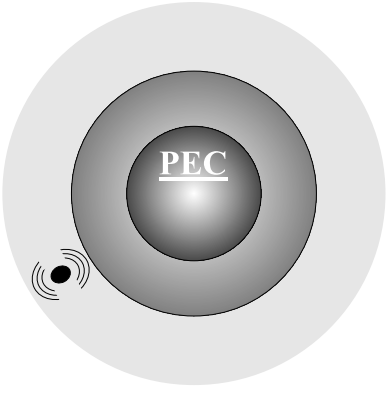

Fig. 10. Propagation of electromagnetic pulse in inhomogeneous media.

In order to obtain the high-order accurate solution of this problem one should overcome a number of difficulties [18]:

(1) Discontinuity in the dielectric permittivity ε. The presence of the interface implies that the Maxwell equations have discontinuous coefficients. The modelled problem can be considered "quasi-one-dimensional" – the discontinuity appears in one direction only. However, our goal is to handle it with the minimal lost of accuracy.
(2) Formulation of artificial boundary conditions to emulate an unbounded domain in the radial direction.
(3) Singularities at the poles. Eqs. (15) and (16) become singular when $\theta = 0, \pi$.
(4) The grid in spherical coordinates is non-uniform and becomes very dense near the poles. The time-step allowed by stability is proportional to $\sin\theta$ which is very small near the poles.

6.2. Numerical scheme

We implement the fourth-order accurate scheme discussed in Section 2. We define the staggered location of the components on the grid and follow this convention in the code. We choose the following location of the components:

$$\begin{aligned}
&E_r \to \{i+1/2, j, k, t\},\\
&E_\theta \to \{i, j+1/2, k, t\},\\
&E_\varphi \to \{i, j, k+1/2, t\},\\
&H_r \to \{i, j+1/2, k+1/2, t+\Delta t/2\},\\
&H_\theta \to \{i+1/2, j, k+1/2, t+\Delta t/2\},\\
&H_\varphi \to \{i+1/2, j+1/2, k, t+\Delta t/2\}.
\end{aligned} \tag{17}$$

6.3. Regularization

Since the discontinuity is only in the r direction we can use a one-dimensional global regularization based on (10) + (11). However, due to the staggering of the spatial stencil (see also (17)) the regularization of ε that appears with each component of electric field should be treated separately. We define ε^r as the permittivity sharing the same grid with E_r, ε^θ is associated with E_θ and ε^φ with E_φ.

The most difficult case to be resolved is when the component is located at the interface, where the associated dielectric permittivity is not defined. This problem is modelled in Section 4. If we put the interface at the node $(i\Delta r)$, then according to (17), such a situation happens with ε^θ and ε^φ. So, both of them are approximated using the global regularization, when the values of ε that appear in RHS of (10) are defined at half-nodes through the entire computational domain.

6.4. Construction of artificial boundary conditions in spherical coordinates

To prevent reflections from the outer artificial boundary in the radial direction we implement a perfectly matched layer (PML). We consider the generalization of the uniaxial PML, derived by Gedney in [8], to spherical coordinates. We convert the Maxwell equations to Fourier space as Teixeira and Chew [23] have suggested:

$$\begin{aligned}
&\mathrm{i}\omega\varepsilon\left(\frac{\tilde r}{r}\right)^2 E_r = \frac{1}{r\sin\theta}\left\{\frac{\partial}{\partial\theta}\left[\sin\theta\left(\frac{\tilde r}{r}H_\varphi\right)\right] - \frac{\partial}{\partial\varphi}\left(\frac{\tilde r}{r}H_\theta\right)\right\},\\
&\mathrm{i}\omega\varepsilon s_r\frac{\tilde r}{r}E_\theta = \frac{1}{r\sin\theta}\frac{\partial}{\partial\varphi}(s_r H_r) - \frac{1}{r}\frac{\partial}{\partial r}\left[r\left(\frac{\tilde r}{r}H_\varphi\right)\right],\\
&\mathrm{i}\omega\varepsilon s_r\frac{\tilde r}{r}E_\varphi = \frac{1}{r}\left\{\frac{\partial}{\partial r}\left[r\left(\frac{\tilde r}{r}H_\theta\right)\right] - \frac{\partial}{\partial\theta}(s_r H_r)\right\},
\end{aligned} \tag{18}$$

where

$$s_r = 1 + \frac{\sigma}{\mathrm{i}\omega}, \quad \sigma^* = \frac{1}{r}\int^r \sigma \,\mathrm{d}r, \quad \frac{\tilde{r}}{r} = 1 + \frac{\sigma^*}{\mathrm{i}\omega}. \tag{19}$$

The two artificial conductivities σ and σ^* are equal to zero inside the physical domain. In the PML region σ and σ^* increase towards the external boundary for instance, as a polynomial. Different profiles have been promoted (see, for instance [9]) for scaling σ. However, the polynomial profile

$$\sigma(x) = \sigma_{\max}\left(\frac{x}{L_{\mathrm{PML}}}\right)^p$$

has proved its effectiveness and it is implemented in many codes. There are three parameters that have to be provided for the polynomial scaling: $L_{\mathrm{PML}} = N\Delta x$ – the thickness of the PML, $\sigma_{\max}$ and p. For larger p, σ grows more rapidly towards the outer boundaries of the PML. In this region the field amplitudes of the waves have sufficiently decayed and so reflections due to the discretization error contribute less. However, if p is too large, the decay of the field emulates a discontinuity and amplifies the wave reflected by the PEC boundary towards the physical domain. We choose $p = 4$, see also [9]. Artificial conductivity σ^* is computed exactly using (19). We introduce new variables:

$$E_r^* = s_r E_r, \quad P_r = \frac{\tilde{r}}{r}E_r, \quad E_\theta^* = \frac{\tilde{r}}{r}E_\theta, \quad E_\varphi^* = \frac{\tilde{r}}{r}E_\varphi$$

and similarly for $\vec{H}$. Substituting this into (18) we have:

$$\begin{aligned}
&(\mathrm{i}\omega\varepsilon + \sigma^*)P_r = \frac{1}{r\sin\theta}\left[\frac{\partial}{\partial\theta}\left(\sin\theta H_\varphi^*\right) - \frac{\partial}{\partial\varphi}(H_\theta^*)\right],\\
&(\mathrm{i}\omega + \sigma^*)E_r^* = (\mathrm{i}\omega + \sigma)P_r,\\
&(\mathrm{i}\omega\varepsilon + \sigma)E_\theta^* = \frac{1}{r\sin\theta}\frac{\partial}{\partial\varphi}H_r^* - \frac{1}{r}\frac{\partial}{\partial r}(rH_\varphi^*),\\
&(\mathrm{i}\omega\varepsilon + \sigma)E_\varphi^* = \frac{1}{r}\left[\frac{\partial}{\partial r}(rH_\theta^*) - \frac{\partial}{\partial\theta}(H_r^*)\right]
\end{aligned} \tag{20}$$

and similarly for $\vec{H}$. We replace $\vec{E}$ by $\vec{E}^*$ and add two variables P_r and Q_r. This is converted to the time-domain using $\mathrm{i}\omega \to \frac{\partial}{\partial t}$. This yields:

$$\begin{aligned}
&\varepsilon\frac{\partial P_r}{\partial t} + \sigma^* P_r = \frac{1}{r\sin\theta}\left[\frac{\partial}{\partial\theta}(\sin\theta H_\varphi^*) - \frac{\partial}{\partial\varphi}(H_\theta^*)\right],\\
&\frac{\partial E_r^*}{\partial t} + \sigma^* E_r^* = \frac{\partial P_r}{\partial t} + \sigma P_r,\\
&\varepsilon\frac{\partial E_\theta^*}{\partial t} + \sigma E_\theta^* = \frac{1}{r\sin\theta}\frac{\partial}{\partial\varphi}H_r^* - \frac{1}{r}\frac{\partial}{\partial r}(rH_\varphi^*),\\
&\varepsilon\frac{\partial E_\varphi^*}{\partial t} + \sigma E_\varphi^* = \frac{1}{r}\left[\frac{\partial}{\partial r}(rH_\theta^*) - \frac{\partial}{\partial\theta}(H_r^*)\right],\\
&\mu\frac{\partial Q_r}{\partial t} + \sigma^* Q_r = -\frac{1}{r\sin\theta}\left[\frac{\partial}{\partial\theta}(\sin\theta E_\varphi^*) - \frac{\partial}{\partial\varphi}(E_\theta^*)\right],\\
&\frac{\partial H_r^*}{\partial t} + \sigma^* H_r^* = \frac{\partial Q_r}{\partial t} + \sigma Q_r,\\
&\mu\frac{\partial H_\theta^*}{\partial t} + \sigma H_\theta^* = -\left[\frac{1}{r\sin\theta}\frac{\partial}{\partial\varphi}E_r^* - \frac{1}{r}\frac{\partial}{\partial r}(rE_\varphi^*)\right],\\
&\mu\frac{\partial H_\varphi^*}{\partial t} + \sigma H_\varphi^* = -\frac{1}{r}\left[\frac{\partial}{\partial r}(rE_\theta^*) - \frac{\partial}{\partial\theta}(E_r^*)\right].
\end{aligned} \tag{21}$$

Inside the physical domain, where $\sigma = \sigma^* \equiv 0$, system (21) is equivalent to (15) ($\vec{E}^* \equiv \vec{E}$ and $\vec{H}^* \equiv \vec{H}$). Hence, we need only 8 variables inside the PML instead of the 12 that were suggested in [23] or 10 that were suggested in [27]. Gedney in [9] derives a spherical uniaxial medium that leads to similar equations to that presented here (there are misprints in the formula in the book).

6.5. Singularity at the poles

Eqs. (15) and (16) become singular when θ is equal to 0 or π. However, this is only a coordinate singularity. In particular we assume that all components of the electric and magnetic fields have at least one continuous derivative at all points including $\theta = 0$ and $\theta = \pi$. Because of the geometry, the solution is independent of φ at the poles and so all derivatives with respect to φ are zero at the poles. This was first analyzed by Holland [13], where he used an integral form of Maxwell equations at the poles to avoid the singularity. We shall use a different approach [21]. The solution can be bounded at the poles both analytically and numerically only if the coefficient $\frac{1}{r\sin\theta}$ is equal to zero. In such a case L'hôpital's rule can be applied. This yields from (15) (when $\theta = 0,\ \pi$):

$$
\begin{aligned}
&E_\varphi = H_\varphi = 0,\\
&\frac{\partial}{\partial r}(rH_\theta) - \frac{\partial H_r}{\partial \theta} = 0,\\
&\frac{\partial}{\partial r}(rE_\theta) - \frac{\partial E_r}{\partial \theta} = 0.
\end{aligned}
$$

Using (16), we get at the poles:

$$
\begin{aligned}
&E_\theta = E_\varphi = H_\theta = H_\varphi = 0,\\
&\frac{\partial E_r}{\partial \theta} = \frac{\partial H_r}{\partial \theta} = 0.
\end{aligned}
$$

Thus, the system (15), when $\theta = 0,\ \pi$, can be written as:

$$
\begin{aligned}
&\varepsilon\tfrac{\partial E_r}{\partial t} = \tfrac{1}{r}\tfrac{\partial H_\phi}{\partial \theta}, \quad && \mu\tfrac{\partial H_r}{\partial t} = -\tfrac{1}{r}\tfrac{\partial E_\phi}{\partial \theta},\\
&E_\theta = 0, && H_\theta = 0,\\
&E_\phi = 0, && H_\phi = 0.
\end{aligned}
\tag{22}
$$

Distributing the grid nodes according to (17) we need to resolve only the E_r component at the poles. We define H_φ as an odd function at $\theta = 0,\ \pi$.

6.6. Fourier filtering

The grid in spherical coordinates is non-uniform and becomes very dense near the pole. The time-step allowed by stability is proportional to $\sin\theta$. To increase the time-step, which can be very small (see for example [10]), we introduce Fourier filtering in the θ direction near the poles (see also [18]) according to the algorithm presented in Fig. 11, where the exponential filter has the form $e^{-2\theta(\tilde{r}+\tilde{\varphi})}$. The 2D FFT is applied in the r and φ directions for fixed θ. Implementation of the algorithm, shown in Fig. 11, requires the determination of several parameters:

- N_f – the frequency of application (in number of iterations).
- N_l – the percentage of θ-layers affected by the filter.
- N_e/N_k – the percentage of frequencies completely eliminated/kept in each layer.

The number of frequencies removed in the θ direction depends on the distance from the pole. Near the pole only a small fraction of the total frequencies are kept, while away from the pole all the allowable discrete modes are kept. This effectively reduces the high frequencies in circular layers near the pole and allows a significant

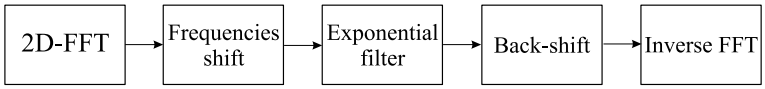

Fig. 11. Algorithm of the Fourier filtering.

increase in the time-step. We have chosen the following set of parameters: $N_f = 10$, $N_l = 25$ (near each pole), N_e decreases from 50% to 0% away from the pole and N_k increases from 34% to 100% away from the pole. This allowed us to increase the time-step by at least a factor of two.

6.7. Graphical representation of results

To check the algorithm described in the previous sections, we consider the following 3D test example. A PEC sphere of radius $r = 1$ is surrounded by two media separated by an interface located 0.5 from the sphere surface. The uniaxial PML is implemented to absorb waves leaving the physical domain. The number of layers is set equal to 12 and the artificial conductivity σ increases as a third degree polynomial. The piecewise continuous dielectric permittivity is regularized using the global regularization approach ((10) + (11)). The media closest to the sphere has a relative dielectric permittivity $\varepsilon_r = 2$ and it is externally bounded by free space ($\varepsilon_r = 1$). The point source, in the form of the Gaussian pulse, is located in free space at a distance 0.75 from the surface of the PEC sphere. To make the results "understandable" we convert the solution to Cartesian coordinates and visualize the solution using Data Explorer. The picture in Fig. 12 shows the E_x component at time $T = 2.8$ (when the waves reach the internal sphere). The unit PEC unit sphere of radius $r = 1$ is centered at $r = 0$ and the source is located at $(-1.66, 0, -0.54)$.

The transparent sphere in Fig. 12 is a sphere filled with PEC. The "red" discus includes the interface and the areas adjacent to it consisting of free space and the dielectric. In this figure one can distinguish between different parts of the solution. For example, E_x inside the transparent (PEC) sphere in the center of the domain and also the red colored oscillations in E_x in the vicinity of the interface.

In Fig. 13 we show a slice of the E_ϕ component in the θ direction (taken at the source). This shows that some of the waves are reflected by the interface. The physical explanation of this phenomena that refraction causes the waves to change direction and to move from the selected slice, needs do be combined with the numerical problem of under-resolution since the Gaussian pulse includes a full spectrum of wavelengths. When the waves travel through a medium with a smaller speed of light then some of the waves can be only be represented on a finer grid.

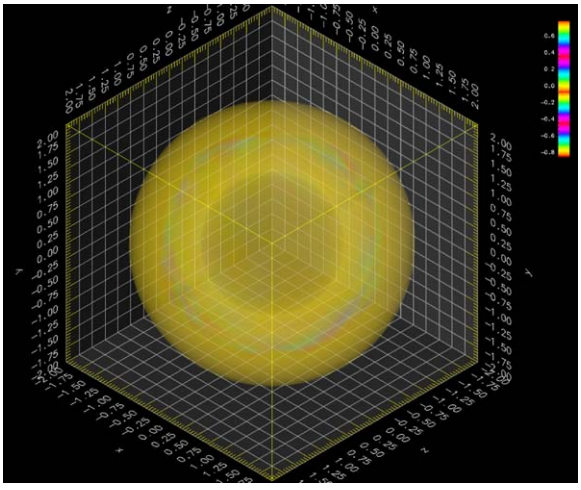

Fig. 12. Converted to Cartesian coordinates. E_x component of the total electric field over entire physical domain.

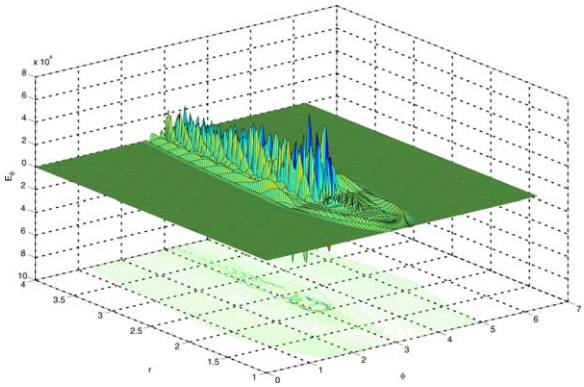

Fig. 13. The slice of E_φ component in θ-direction, taken at source point.

7. Concluding remarks

We have performed detailed computations for the time-dependent Maxwell system in one dimension with a discontinuity in some of the coefficients across the interfaces between the media. We use a compact implicit fourth-order accurate method on a staggered grid to solve the equations.

We show that regularization can be considered a reasonable approach to the solution of the Maxwell equations with discontinuous coefficients. The global regularization based on an implicit (Padé) interpolation yields almost third-order accuracy, which is one order less than the basic accuracy of the scheme. A drawback of the global regularization is the reduction of the CFL constant for large jumps in the discontinuities. Local regularization does not require a reduction of the time-step, however, it reduces the global accuracy of the algorithm to second-order. An application of the regularization techniques and the high-order accurate finite difference algorithm is a very effective tool for the modelling photonic band gaps (PBG) (see, for instance, [17]) and other phenomena rising from electromagnetic wave propagation through periodic dielectric structures.

For problems in a spherical coordinate system we regularize ε in the r direction. We Fourier transform the variables and then remove the higher frequencies near the poles. This allows the use of a larger time-step. A PML in the far field is used to reduce reflections back into the domain. We use L'hôpital's rule to derive boundary conditions at the poles.

Future work will extend this to the scattering of electromagnetic waves by multi-dimensional dielectric bodies that are not aligned with the mesh.

References

[1] U. Andersson, Time-Domain Methods for the Maxwell's Equations, Ph.D. Thesis, Royal Institute of Technology, Sweden, 2001.
[2] U. Andersson, B. Engquist, Regularization of material interfaces for finite difference methods for the Maxwell equations, Report 2002-01, Parallel and Sci. Comp. Inst. Royal Institute of Technology and Uppsala University, 2002.
[3] W. Cai, S. Dong, An upwinding embedded boundary method for Maxwell's equations in media with material interfaces: 2-D case, J. Comput. Phys. 19 (1) (2003) 159–183.
[4] A.C. Cangellaris, D.B. Wright, Analysis of the numerical error caused by the stair-stepped approximation of a conducting boundary in FDTD simulations of electromagnetic phenomena, IEEE Trans. Antenn. Propag. 39 (10) (1991) 1518–1525.
[5] M.H. Carpenter, D. Gottlieb, S. Abarbanel, The stability of numerical boundary treatments for compact high-order finite difference schemes, J. Comput. Phys. 108 (2) (1993) 541–559.
[6] M.H. Carpenter, D. Gottlieb, S. Abarbanel, Stable and accurate boundary treatment for compact high-order finite difference scheme, Appl. Numer. Anal. 12 (1993) 55–81.
[7] K.H. Dridi, J.S. Hesthaven, A. Ditkowski, Staircase-free finite-difference time-domain formulation for general materials in complex geometries, IEEE Trans. Antenn. Propag. 49 (5) (2001) 749–756.
[8] S.D. Gedney, An anisotropic perfectly matched layer-absorbing medium for the truncation of FDTD lattices, IEEE Trans. Antenn. Propag. 4 (12) (1996) 1630–1639.
[9] S.D. Gedney, The perfectly matched layer absorbing medium, in: A. Taflove (Ed.), Advances in Computational Electrodynamics: The Finite-Difference Time-Domain Method, Artech House, Boston, MA, 1998, pp. 263–344 (Chapter 5).

[10] S.D. Gedney, J.A. Roden, N.K. Madsen, A.H. Mohammadian, W.F. Hall, V. Shankar, C. Rowell, Explicit time-domain solutions of Maxwell's equations via generalized grids, in: A. Taflove (Ed.), Advances in Computational Electrodynamics: The Finite-Difference Time-Domain Method, Artech House, Boston, MA, 1998, pp. 163–262 (Chapter 4).
[11] D. Gottlieb, B. Yang, Comparisons of staggered and non-staggered schemes for Maxwell's equations, in: 12th Annual Review of Progress in Applied Computational Electromagnetics, Monterey, CA, 1996, pp. 1122–1131.
[12] J.S. Hesthaven, High-order accurate methods in time-domain computational electromagnetics. A review, Adv. Imaging Electron Phys. 127 (2003) 59–123.
[13] R. Holland, THREDS: A finite-difference time-domain EMP code in 3D spherical coordinates, IEEE Trans. Nucl. Sci. NS-30 (1983) 4592–4595.
[14] R. Holland, Pitfalls of staircase meshing, IEEE Trans. Electromag. Compat. 35 (1993) 434–439.
[15] J.M. Hyman, Accurate monotonicity preserving cubic interpolation, SIAM J. Sci. Stat. Comput. 4 (1983) 645–654.
[16] B. Jiang, J. Wu, L.A. Povinelli, The origin of spurious solutions in computational electromagnetics, J. Comput. Phys. 125 (1996) 104–123.
[17] J.D. Joannopoulos, R.D. Meade, J.N. Winn, Photonic Crystals: Molding the Flow of Light, Princeton University Press, Princeton, NJ, 1995.
[18] E. Kashdan, High-Order Accurate Methods for Maxwell Equations, Ph.D. Thesis, Tel Aviv University, 2004.
[19] E. Kashdan, B. Galanti, A new parallelization strategy for solution of the time-dependent three-dimensional Maxwell's equations using a high-order accurate compact implicit scheme, Int. J. Numer. Model. (submitted for publication).
[20] E. Kashdan, E. Turkel, A high order accurate method for frequency domain Maxwell equations with discontinuous coefficients, J. Sci. Comput. (2006). doi:10.1007/s10915-005-9049-5.
[21] E. Kashdan, E. Turkel, Numerical solution of Maxwell's equations in spherical coordinates, in: 19th Annual Review of Progress in Applied Computational Electromagnetics, Monterey, CA, March, 2003, pp. 188–192.
[22] A. Taflove, S.C. Hagness, Computational Electrodynamics: The Finite-Difference Time-Domain Method, third ed., Artech House, Norwood, MA, 2005.
[23] F.L. Teixeira, W.C. Chew, Systematic derivation of anisotropic PML absorbing media in cylindrical and spherical coordinates, IEEE Microwave Guided Wave Lett. 7 (11) (1997) 371–373.
[24] A.K. Tornberg, B. Engquist, Regularization techniques for numerical approximation of PDEs with singularities, J. Sci. Comput. 19 (2003) 527–552.
[25] E. Turkel, High-order methods, in: A. Taflove (Ed.), Advances in Computational Electrodynamics: The Finite-Difference Time-Domain Method, Artech House, Boston, MA, 1998, pp. 63–110 (Chapter 2).
[26] E. Turkel, A. Yefet, Fourth order method for Maxwell's equations on a staggered mesh, in: IEEE Antennas Propagation Society, International Symposium, Montréal, Canada, 1997, pp. 2156–2159.
[27] B. Yang, P.G. Petropoulos, Plane-wave analysis and comparision of split-field, biaxial and uniaxial PML methods as ABCs for pseudospectral electromagnetic wave simulation in curvilinear coordinates, J. Comput. Phys. 146 (1998) 747–774.
[28] K.S. Yee, Numerical solution of initial boundary value problems involving Maxwell's equations in isotropic media, IEEE Trans. Antenn. Propag. 1 (3) (1966) 302–307.
[29] A. Yefet, Fourth Order Accurate Compact Implicit Method for the Maxwell Equations, Ph.D. Thesis, Tel Aviv Univ, 1998.
[30] A. Yefet, E. Turkel, Fourth order compact implicit method for the Maxwell equations with discontinuous coefficients, Appl. Numer. Math. 33 (2000) 125–134.
[31] D.W. Zingg, T.T. Chisholm, Runge–Kutta methods for linear problems, in: Proceedings of 12th AIAA Comp. Fluid Dynamics Conference, 1995.